

On the formation of cold fronts in massive mergers

H. Mathis^{1*}, G. Lavaux^{1,2}, J. M. Diego¹, J. Silk¹

¹*University of Oxford, Astrophysics, Denys Wilkinson Building, Keble Road, Oxford OX1 3RH, UK*

²*Ecole Normale Supérieure de Cachan, Avenue du Président Wilson, 94230 Cachan, France*

2 April 2018

ABSTRACT

Using adiabatic hydrodynamical simulations, we follow the evolution of two symmetric cold fronts developing in the remnant of a violent $z = 0.3$ massive cluster merger. The structure and location of the simulated cold fronts are very similar to those recently found in X-ray cluster observations, supporting the merger hypothesis for the origin of at least some of the cold fronts. The cold fronts are preceded by an almost spherical bow shock which originates at the core and disappears after 1.6 Gyr. The cold fronts last longer and survive until $z \sim 0$. We trace back the gas mass constituting the fronts and find it initially associated with the two dense cores of the merging clusters. Conversely, we follow how the energy of the gas of the initial merging cores evolves until $z = 0$ from the merging and show that a fraction of this gas can escape from the local potential well of the sub-clumps. This release occurs as the sub-clumps reach their apocentre in an eccentric orbit and is due to decoupling between the dark matter and part of the gas in the sub-clump because of, first, heating of the gas at first close core passage and of, second, the effect of the global cluster pressure which peaks as the centrifugal acceleration of the sub-clump is maximal. The fraction of the gas of the sub-clump liberated in the outbound direction then cools as it expands adiabatically and constitutes the cold fronts.

Key words: hydrodynamics – shock waves – galaxies: clusters: general – intergalactic medium

1 INTRODUCTION

High resolution X-ray temperature images obtained by *Chandra* of the intracluster medium (ICM) show that large, cold regions in pressure equilibrium with their surrounding medium are a very common phenomenon in massive clusters (Markevitch et al. 2000, but also Vikhlinin et al. 2001; Mazzotta et al. 2001; Sun et al. 2002; Markevitch & Vikhlinin 2001). Their high gas density largely compensates for the factor of 1.3 to 4 drop in temperature so that their X-ray surface brightness is still typically higher than the rest of the ICM. The whole cold region is commonly referred to as a “cold front”, even if the term would strictly only describe a possible upstream contact interface of the cold gas with the hot ICM.

Employing the term in its loose sense, these cold fronts are extended structures with sizes of one hundred to a few hundred kpc, observed up to a significant fraction of the virial radius; X-ray maps show that cold fronts are preceded by bow shocks (Vikhlinin & Markevitch 2002; Markevitch

et al. 2002a). They differ from very dense clumps of gas orbiting the ICM which extend to a few tens of kpc at most. These clumps are much more difficult to observe except in the central regions of clusters (Fujita et al. 2002), and they are expected to be the direct remnants of the cores of massive haloes that have merged with the cluster. However, cold sub-clumps would share two similar characteristics with cold fronts: a high X-ray surface brightness and pressure equilibrium with the ICM.

Numerical simulations have already addressed the formation of cold fronts: in a pioneering simulations of merging clusters of galaxies using Eulerian hydrodynamics, Roettiger et al. (1997) studied cluster-subcluster idealised mergers, and showed that substructure, shocks and adiabatic cooling could result in a complex temperature map.

More recently, Ricker & Sarazin (2001) have addressed the evolution of the X-ray luminosity and temperature of the ICM in a series of off-axis mergers of idealised subclusters. They show that the overall luminosity and temperature increase due to merging shocks and regions of gas compression which are observationally unresolved can strongly bias the cluster mass if it is derived assuming a non-merging cluster.

Nagai & Kravtsov (2003) and Bialek et al. (2002) have

* hxm@astro.ox.ac.uk

shown that cold fronts like those found by Markevitch et al. (2000) can form as a result of massive mergers in a cosmological setting. While both clearly stated that their simulated cold fronts occur when “the subcluster gas strays from its local potential minimum and expands adiabatically” they did not explain the process in detail. Nevertheless, they pointed out that further observations and simulations need to be carried out to assess how frequently cold fronts may occur in massive mergers. In fact, massive mergers need not be the only process responsible for cold fronts, but they may be sufficient even at low redshift to explain their observed abundance, all the more if they can remain stable within the ICM for a sufficiently long time. In a recent paper, Heinz et al. (2003) have considered ram pressure stripping as a possible mechanism for forming some of the cold fronts. They do not include dark matter in their simulations, but study the partial unbinding of a dense clump of gas undergoing stripping from an external, uniform wind switched on at the beginning of the simulation, representing the surrounding ICM. This process may be complementary but is not identical to the one we will focus on.

In the present paper, we study the occurrence of cold fronts as a possible result of a major merger, focusing on the interplay between the dark matter and the gas of the sub-cluster cores orbiting in the newly formed ICM. Like Nagai & Kravtsov (2003) and Bialek et al. (2002), we follow the late formation of a massive cluster in the Λ CDM cosmology using hydrodynamical adiabatic simulations. We employ an entropy-conserving DM+SPH scheme which is suitable to follow the Lagrangian evolution of the flow and the history of the gas of the cold front. We set the initial conditions to merge two equal mass haloes into a massive, but plausible, $1.4 \times 10^{15} M_{\odot}$ final object to more easily bring out the interesting features.

Our massive merger takes place at $z = 0.3$. It produces by $z = 0.2$ two cold fronts which develop in a 500 kpc thick plane containing the orbits of the two merging cores and expand in the wake of an almost spherically symmetric “bow shock”. This bow shock results from the transonic motion of the merging subcluster cores in the ICM. The medium may have been previously partly heated by a merger shock due to the compression of the gas between the subcluster cores in their convergent motion before their first encounter. The dense gas cores of the two merging halos survive until close to the present time, when they eventually merge. As the cores orbit in the merger remnant, the gas within them is first strongly heated up adiabatically at pericentre by the variation of the gravitational potential due to close encounter, it then cools down partly though not symmetrically between core passage and apocentre as the potential increases again, before it is finally heated up by the final inspiralling.

While a fraction of gas particles of the sub-clumps is tidally stripped at the first closest encounter, both cold fronts form later, at the apocentre of the sub-clumps orbits. We show that the fronts consist of some of those gas particles initially within the dense cores which can escape out of the local gravitational potential of the sub-clumps. In our simulation, the cold front phenomenon takes place as the gas of the dense cores is in slight phase advance relative to the dark matter along the outbound part of the orbit, and phase delay relative to the dark matter along the inbound

part. At apocentre in an eccentric orbit, when motions are slower but centrifugal acceleration is high, the overall pressure inside the cluster acts most strongly, in a direction opposite to the gravitational pull. This introduces differences between the dynamical evolution of the gas of the sub-clump and that of the dark matter. They are sufficient to result in liberation of gas which has been compressed and heated at core passage but has not cooled down symmetrically since then. As the cold dense gas leaves the local gravitational potential with high pressure, it expands adiabatically and cools down further. Gas which is expelled in the direction of motion constitutes the cold front. This gas is not later recaptured by the local gravitational potential of the dark matter subclump.

We confirm that the relatively small fraction of the gas mass leaving the local gravitational potential by this process can make the presence of cold fronts in X-ray images very dependent on the mass of the sub-clumps, if cold fronts are mainly produced by the process we describe here. We find that the lifetime of our simulated cold fronts exceeds the time required for the bow shock to travel to the virial radius.

This paper is organised as follows: in Section 2 we present the simulations. In Section 3 we discuss qualitatively the evolution of post-merger physical quantities of the ICM as they are directly available from the simulations. Sections 4 and 5 tackle quantitative aspects of the development of the two main features apparent on the maps: first, merger shocks and bow shocks, and second, cold fronts. Section 6 focuses on one of the two cold fronts, proposes a physical explanation for its origin, and briefly compares to other work. We summarise and conclude in Section 7.

2 OBTAINING A MASSIVE CLUSTER MERGER

2.1 Initial conditions

We assume a concordance Λ CDM cosmology with parameters $\Omega_0 = 0.3$, $\Omega_b h^2 = 0.019$, $\Lambda = 0.7$, $h = 0.7$. To study a major merger, as an alternative to resimulating at higher resolution a cluster selected from a low resolution simulation, we directly constrain the initial gaussian density field so that it has the usual CDM power spectrum but encapsulates information on where and how the $z = 0$ target cluster should form. For this purpose we use the van de Weygaert & Bertschinger (1996) implementation of the Hoffman-Ribak algorithm. We want an equal-mass massive merger to take place at $z \simeq 0.5$; this is obtained if we constrain the initial density field so that it has two gaussian peaks of standard deviation $r = 5$ Mpc, with the same amplitude $A = 5.3 \times \sigma_r$ (where σ_r is the root mean square value of the unconstrained initial density field when smoothed with a gaussian kernel of standard deviation r) and separation $s = 27$ Mpc. Note that constraining the initial velocities of these peaks adds but little control over the final merger at the expense of additional tuning, so we have only used the densities. The above setup results in a very massive, $2 \times 10^{15} M_{\odot}$ cluster at $z = 0$ which follows an NFW density profile, and which formed in an equal-mass merger of two Virgo-sized clusters at $z_{\text{merg}} = 0.3$. Note that z_{merg} is the epoch when the friends-of-friends groupfinder with linking length 0.2 times the mean DM interparticle separation merges the two clusters.

2.2 Simulation details

We employ 2×128^3 DM and SPH particles in a 100 Mpc box and start the simulation at $z_{\text{start}} = 100$. The DM and SPH particle masses and softening lengths read $M_{\text{DM}} = 7.3 \times 10^8 M_{\odot}$ and $M_{\text{SPH}} = 1.3 \times 10^8 M_{\odot}$, and $r_{\text{soft,DM}} = r_{\text{soft,SPH}} = 40$ kpc respectively. The softening lengths are kept fixed throughout in comoving coordinates. The equations of motion are integrated with the public version of GADGET (Springel et al. 2001)[†] which we modified to include the “standard” entropy conservation scheme suggested by Springel & Hernquist (2002). The gas is single-phase, monoatomic with adiabatic index $\gamma = 5/3$ and obeys a perfect gas equation of state. To estimate the sound speed of the ICM, we assume a mean particle mass $\bar{\mu} m_p$ with $\bar{\mu} = 0.59$ and m_p is the proton mass. We do not include cooling, heating, thermal conduction, magnetic fields, nor mechanical or thermal AGN/supernova feedback as our focus is the capability of a massive merger to induce large, long-lasting cold fronts even in an adiabatic evolution. We focus on 11 outputs equally spaced between z_{merg} and $z = 0.1$, and 3 outputs at $z = 0.06$, $z = 0.03$ and $z = 0$. The final virial mass and radius of the cluster, where the enclosed DM density drops to 200 times the critical density, are $m_{\text{vir}} = 1.35 \times 10^{15} M_{\odot}$ and $r_{\text{vir}} = 3.4$ Mpc.

Figure 1 gives the projected DM density of the whole box, with the cluster at the centre. The size of the region shown is 100 Mpc, and the whole box has been projected. The two massive subclusters merging at $z = 0.3$ infall along the diagonal filament spanning from the lower left to the upper right. Once it has formed, the cluster still accretes smaller clumps of DM, mostly from the filament.

2.3 Tracking the cores of the merging subclusters

The merger occurring at $z = 0.3$ involves two subclusters of fairly similar, Virgo-size masses. Following Bialek et al. (2002), we select their two cores (both gas and DM) before z_{merg} , using a linking length 0.05 times the mean interparticle separation. We find that the trajectory of the cores of the subclusters is roughly confined to a constant z slab with thickness 500 kpc, from z_{merg} down to $z = 0$ where they completely mix. Figure 4 shows the particles of the two gas cores projected along the z -direction, over a series of snapshots. The cores have a first close encounter with small impact parameter at $z = 0.2$, reach their apocentre, and finally mix up at $z = 0$. We label as subcluster 1 and 2 the halos approaching at z_{merg} from the lower left corner (in black) and upper right (red) corners respectively. In the following discussion, we will refer to CG_1 (resp. CDM_1) and CG_2 (CDM_2) as the gas (DM) of the two subcluster cores. The resulting number of particles and masses of the two cores are $N_{\text{DM},1} = 12500$, $N_{\text{SPH},1} = 10200$, $M_{\text{DM},1} = 1.5 \times 10^{14} M_{\odot}$, $M_{\text{SPH},1} = 1.7 \times 10^{13} M_{\odot}$ and $N_{\text{DM},2} = 10500$, $N_{\text{SPH},2} = 7200$, $M_{\text{DM},2} = 0.9 \times 10^{14} M_{\odot}$, $M_{\text{SPH},2} = 0.96 \times 10^{13} M_{\odot}$ respectively. Figs. 2 and 3 respectively give the position and velocity of the centres of mass of the gas and dark matter component of the core of the subcluster accreting from the lower left of the simulation (CG_1 and CDM_1 correspond to

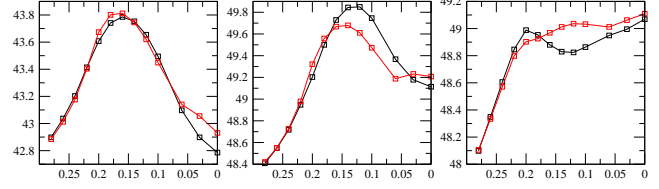


Figure 2. The black and red lines show the spatial evolution after $z_{\text{merg}} = 0.3$ of the centre of mass of the gas and dark matter (respectively) of the core of the subcluster which was accreted from the lower left of the simulation (CG_1 , CDM_1). Left, middle and right panels corresponds to the x -, y - and z -positions. Note how the centre of mass of the gas is offset to the outer parts of the cluster with respect to the centre of mass of the DM in y coordinates at $z = 0.12$ by ~ 200 kpc: the dark matter has already fallen back towards the centre while the gas clump is still stationary: the upper right cold front appears at this point. Note also that the $z \sim 0.2$ delay of the centre of mass of the gas with respect to that of the dark matter may be a consequence of the pressure gradients as core passage takes place then.

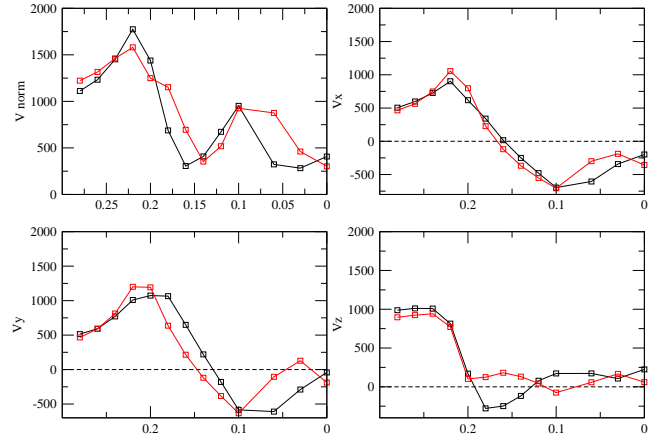


Figure 3. The black and red lines show the evolution after $z_{\text{merg}} = 0.3$ of the velocity of the centre of mass of the gas and dark matter respectively of the core of the subcluster accreted from the lower left of the simulation. The top left panel shows the amplitude of the 3D velocity, while the upper right, lower left and lower right panels respectively give v_x , v_y and v_z . Velocity is transonic at $z \sim 0.21$. Negative accelerations along the x and y directions peak at $z \sim 0.17$.

the black and red curves). Note in Fig. 2 how the centres of mass of the two components of the sub-clump are confined to a thin slab normal to the z -direction. Note also the strong deceleration in v_x and v_y seen around $z = 0.17$ in the top right and bottom left panels of Fig. 3, as the clump reaches the apocentre of its orbit.

3 POST-MERGER EVOLUTION OF THE ICM

In this Section, we track the post-merger evolution of the ICM using maps of a 6×6 Mpc slice cut in the x - y plane of the simulation and centred on the most bound DM particle of the cluster at $z = 0$. Here and in all the following the spatial analysis of the plots and the discussion are in comoving length. The slice is 500 kpc thick and also centred in the z direction. All quantities are projected along the line of sight,

[†] <http://www.mpa-garching.mpg.de/~volker/gadget>

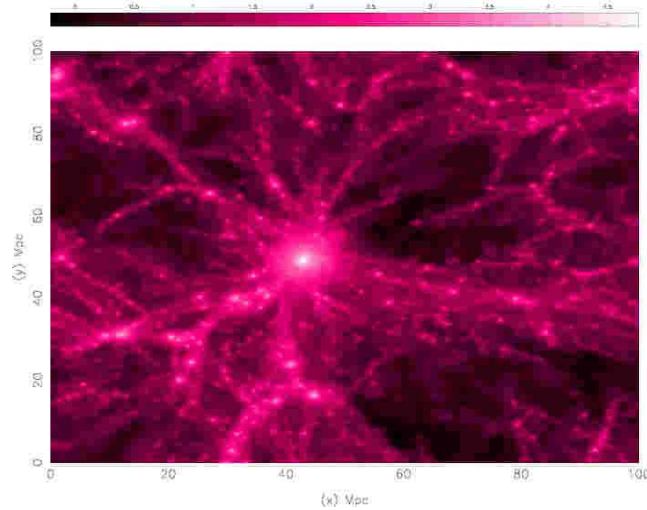


Figure 1. Projected $z = 0$ gas density of the simulation. The region shown is 100 Mpc wide and we have projected a 10 Mpc thick slice normal to the z direction and centred on the cluster. The densities are colour-coded logarithmically. The cluster hosting the cold fronts, at the centre of the image, appears well relaxed, but note that the spatial and dynamic range chosen here make it difficult to fully render the substructure of the cluster. A better, high resolution version of this figure is available at: <http://www-astro.physics.ox.ac.uk/~hxm/ColdFronts/>.

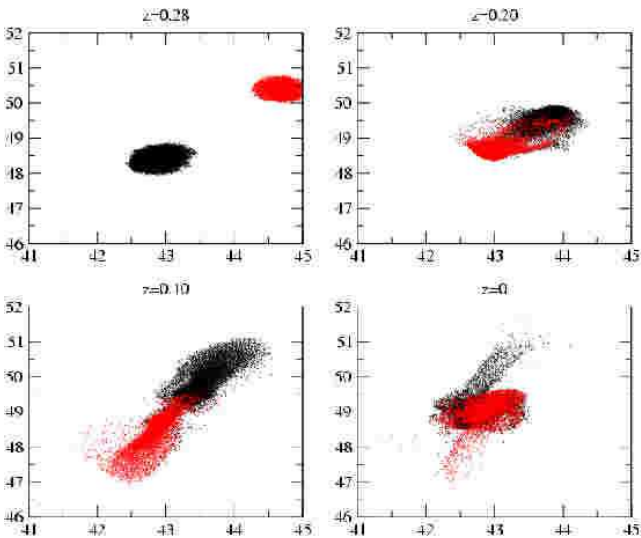


Figure 4. Positions of the gas particles of the clumps CG_1 (black) and CG_2 (red) at four different redshifts in the x - y plane. The particles have been selected using a friends-of-friends groupfinder and their evolution was tracked down. The window is the same for the four plots. A better, high resolution version of this figure is available at: <http://www-astro.physics.ox.ac.uk/~hxm/ColdFronts/>.

i.e. in the z -direction. Due to the small thickness of the slice, we expect only minor blurring because of projection effects. While temperature and pressure fully describe the thermodynamics of the gas, both observable as respectively, the X-ray emission-weighted temperature and the Compton y parameter, the specific entropy, although not directly observable enables one to trace non-adiabatic phenomena like shocks and has become widely used in studies of the ICM.

Figures 5, 6 and 7 show consecutive maps of, respectively, the bremsstrahlung-emission-weighted temperature of the ICM, the Compton y parameter and, following com-

mon practice, the adiabat $A(s)$ of the gas defined as $P = A(s)\rho^\gamma$. $A(s)$ is a monotonic function of the specific entropy of the gas, and it is related to the formal thermodynamic entropy per particle s as: $A(s) = e^{2/3(s-s_0)}$ where s_0 depends only on fundamental constants and on the mixture of particle masses (Voit et al. 2003). We divide the full sequence in three consecutive phases: first, the initial compression of the intervening gas, between z_{merge} and $z = 0.22$, second, the generation of the cold fronts, from $z = 0.2$ to $z = 0.12$, and third, the final relaxation from $z = 0.1$ to $z = 0$. We only give a qualitative description and we postpone the quantitative analysis to the following two sections. To conclude this section, we give X-ray luminosity maps in four typical configurations to show resemblance to the observations.

3.1 Compression of the intervening gas

The first four panels of Figs. 5 to 7 show how the intracluster gas between the two subcluster cores is compressed and shock heated as they approach the centre from the lower left and upper right corners respectively. The compression at the centre of the forming cluster is obvious in the temperature maps (Fig. 5) where a slab of hot gas normal to the axis of merging of the subcluster builds up and starts to expand. The top panel of figure 5 of Markevitch et al. (2000) presents a schematic picture of the first stage of a massive merger that they use to model their *Chandra* observation of A2142. (This picture was first derived from simulations by Roettiger et al. 1997 and later confirmed by Ricker & Sarazin 2001.) Following their view, the compression we find would eventually lead to the formation of a merger shock. At $z = 0.22$, the dumbbell pattern visible on the temperature maps is a direct consequence of the dense cool cores compressing the hot gas. Note that Fig. 7 also clearly shows at $z = 0.22$ the location of the subcluster cores as they host the lowest entropy gas of the map. Note also that the absence of subcluster cores in the $z = 0.26$ panels of the Compton y

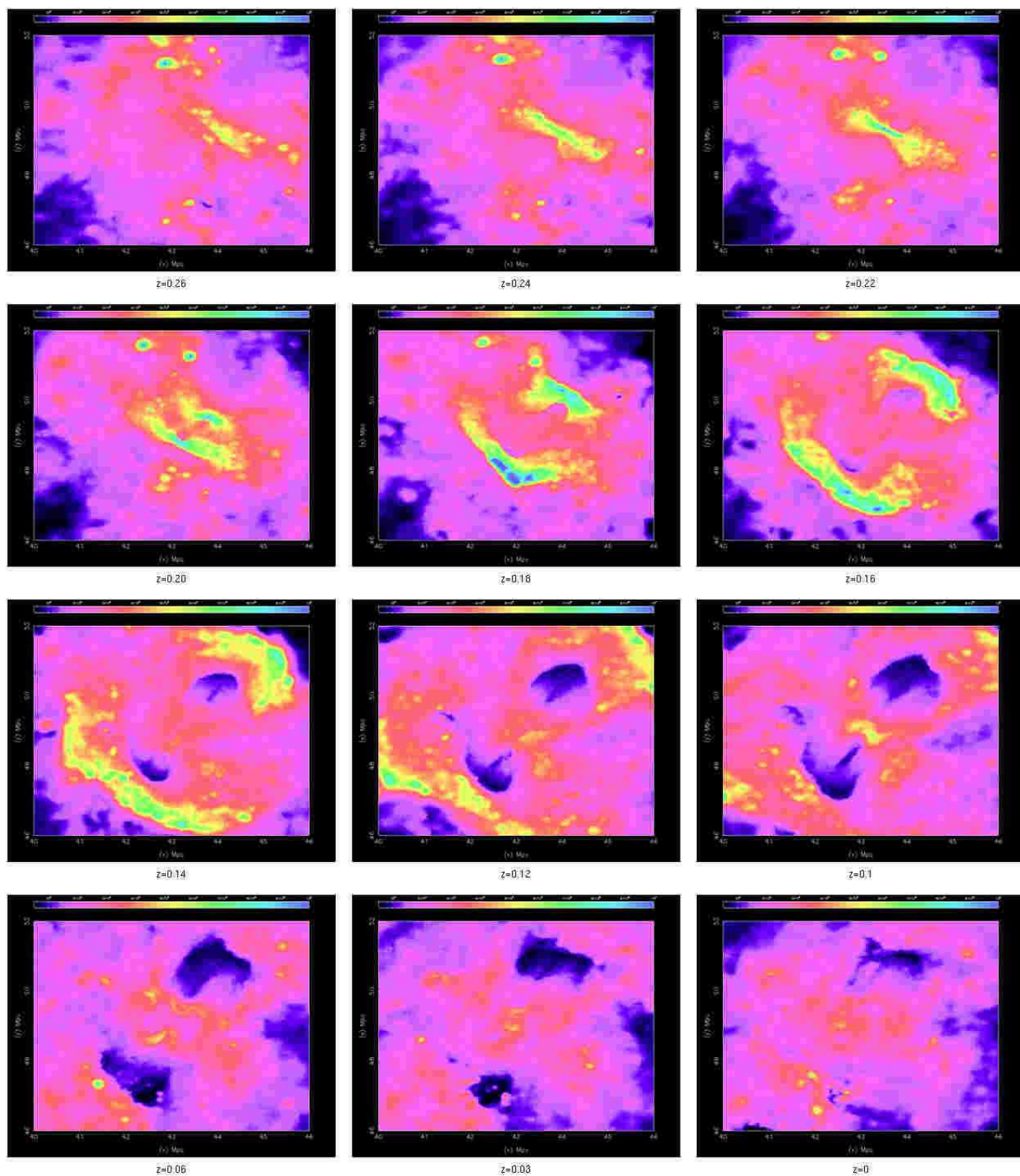


Figure 5. Series of snapshots, from $z = 0.26$ (top left panel) to $z = 0$ (bottom right panel) of the X-ray emission-weighted temperature integrated over a 500 kpc thick slice. Each image shows the same 6×6 Mpc region in the x-y plane. The temperatures are colour-coded linearly and the palette is chosen to emphasise the luminosity contrast for low temperatures. The colour scale ranges from 10^8 to 10^9 K and it is the same for all snapshots. A better, high resolution version of this figure is available at: <http://www-astro.physics.ox.ac.uk/~hxm/ColdFronts/>.

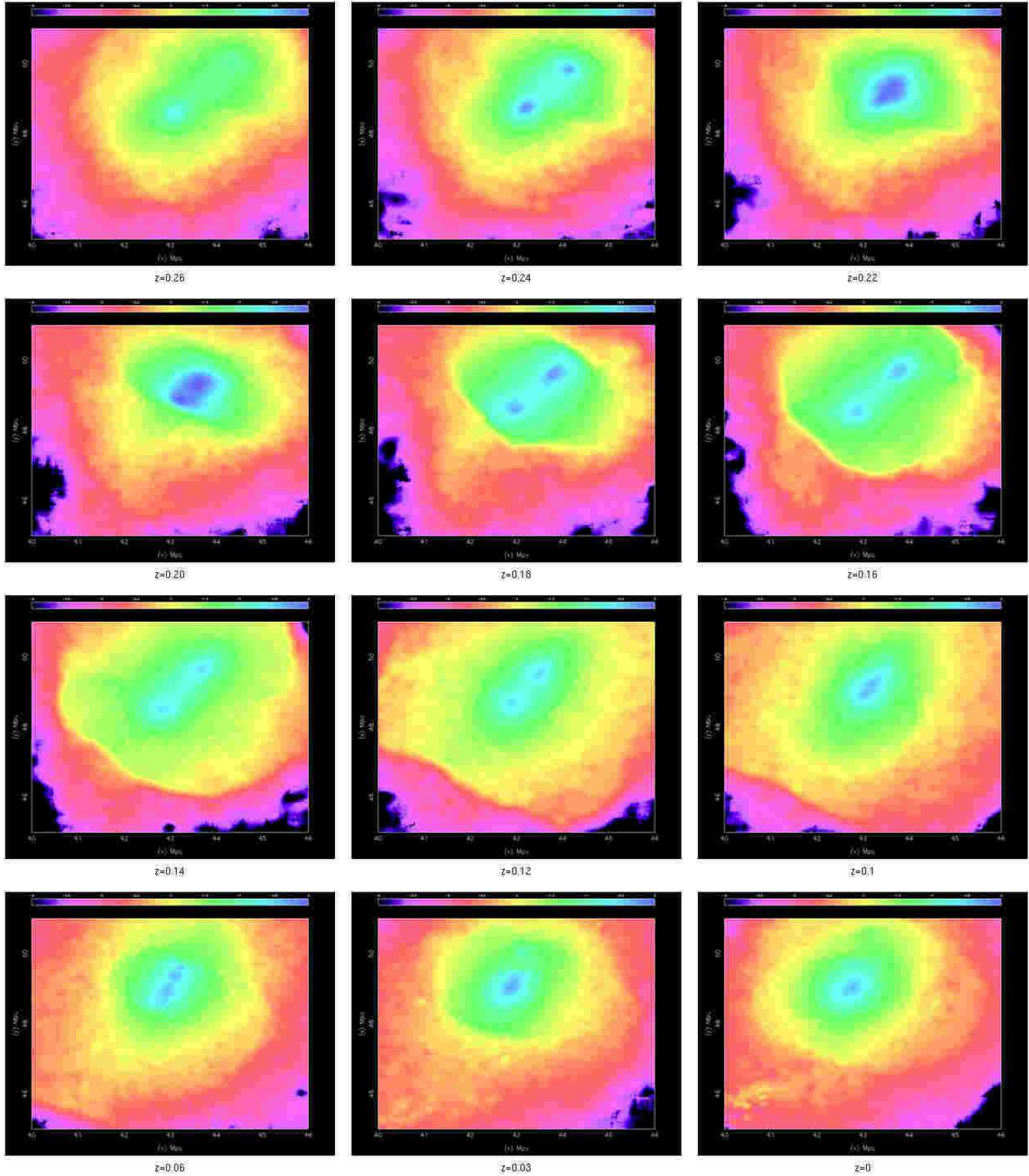


Figure 6. Same as Fig. 5, but for the Compton y parameter of the gas integrated over the 500 kpc thick slice. The colour scale is logarithmic and the normalisation is arbitrary. A better, high resolution version of this figure is available at: <http://www-astro.physics.ox.ac.uk/~hxm/ColdFronts/>.

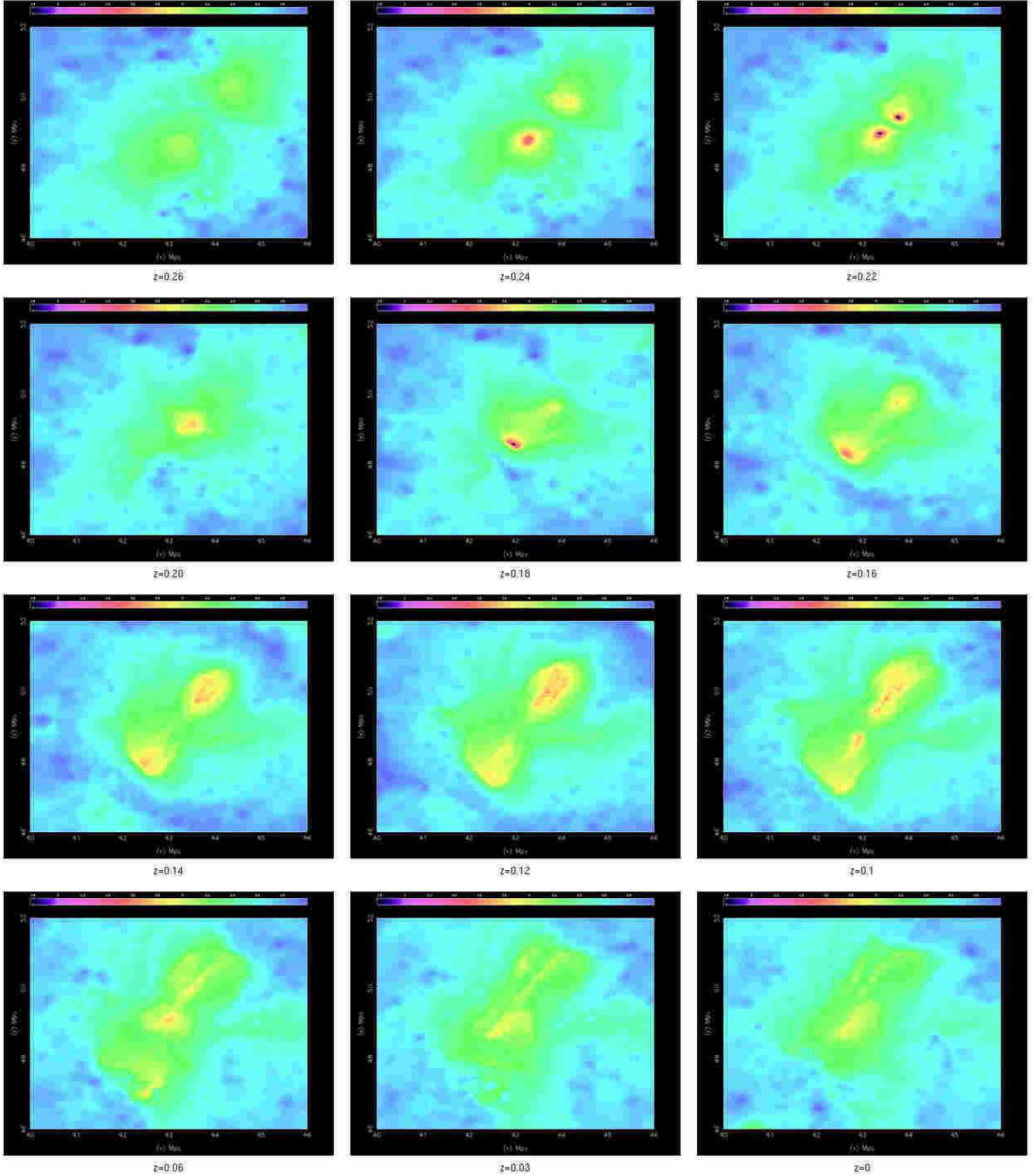


Figure 7. Same as Fig. 5, but for the decimal logarithm of the adiabat $A(s)$. The colour scale is here a linear function of the specific entropy of the gas. A better, high resolution version of this figure is available at: <http://www-astro.physics.ox.ac.uk/~hxm/ColdFronts/>.

parameter and of the entropy (Figs. 6 and 7) is simply due to the two cores being slightly out of the slice chosen for the maps: they reappear by $z = 0.24$.

In our simulation, merger shocks would take place in the ICM as the subcluster gas surrounding one core and

carried out in its motion hits the gas of the other subcluster with opposite direction of motion and supersonic relative velocities. At $z = 0.22$, CG_1 and CG_2 have velocities of order 1700 km/s with respect to the rest-frame of the simulations (twice this for their relative velocity, see the upper

left panel of Fig. 3). The speed of sound in the unshocked ICM is of the same order as the velocity of one clump for a 10^8K ICM (1530 km s^{-1}) and higher for $2 \times 10^8\text{K}$ (2160 km s^{-1}). Shocks are therefore expected to develop; in the following, we will refer to these pre-encounter shocks as “merger shocks”. We will see that they are difficult to follow as they soon correlate to other phenomena.

3.2 Generating the cold fronts

The merger shocks expand from the central regions into the ICM as the subcluster cores go past one another. At $z = 0.2$, the fourth panel of Fig. 5 shows the first stage of expansion of the merger shocks, propagating at close to the speed of sound in the ICM. However, as foreseen by Markevitch et al. (2000) (see the lower panel of their fig. 5), while the subcluster cores head towards their apocentre, they create new shocks as they move in the central cluster regions where the gas has been previously heated by the merger shocks. We will refer to this new set of shocks as “bow shocks”. The bow shocks propagate out at speeds set by the bulk velocities of the sub-clumps, when their motion is supersonic, and become pressure waves propagating at the speed of sound when the motion of the clumps in the surrounding ICM becomes subsonic. In fact, they seem to catch up with the merger shocks in the $z = 0.18$ panel of Fig. 5, where they interfere and make a complex structure. We will consider for simplicity that together they can be described by only one shock wave, and we will not resolve its inner details. In a pattern similar to a temperature annulus, the shock/pressure wave expands up to the virial radius until $z = 0.12$, and it dissolves later in the far outskirts of the cluster (IGM, filaments) not seen on the maps. The birth of the bow shocks is clearly seen in the $z = 0.20$ panel of the Compton y parameter (Fig. 6): the steep pressure rise due to the bow shock appears at the lower left edge of the central light blue zone. The pressure gradient is visible at $z = 0.18$ and even more at $z = 0.16$ where it clearly delineates both lower left and upper right shocks (or pressure waves). Entropy maps (Fig. 7) mainly trace the positions of the subcluster cores and show how they lose a fraction of their low entropy gas to the central region of the cluster after their first crossing, even before reaching the apocentre. The entropy rise due to shocks is less visible however, because we expect a small increase due to shocks in the units we express the entropy: a shock with upstream Mach number $M = 1.4$ (2.2) result in a 1 (10) percent change in $\log A(s)$. We will tackle more quantitative aspects of the shocks in the next section.

Fig. 5 shows little temperature variation between the up- and downstream flows (excluding the broad shock region), at $z = 0.18$ and at $z = 0.16$. This is due to the adiabatic outward expansion of the gas in the downstream region. Two symmetric cold fronts develop in the wake of the bow shocks: while the bottom left front already becomes visible on the temperature map (Fig. 5) at $z = 0.18$, both reach their final position by $z = 0.12$, where they strongly resemble the bow-shaped features of high surface brightness observed in the high resolution X-ray images (see, e.g., the top left panel of figure 4 in Markevitch et al. 2002b). Continuity of the Compton y parameter over the cold fronts is already demonstrated in Fig. 6. The entropy profiles (Fig. 7)

indicate that cold fronts are primarily made of low entropy gas, and we will probe the origin of this gas in Sections 5 and 6. Note the persistence of a filament of low-entropy gas joining the two sub-clump cores from $z = 0.16$ down to $z = 0.10$. This filament traces continuous gas accretion on the central region of the gas particles of CG_1 , CG_2 which have been unbound at first close encounter of the cores and of gas which is gradually stripped off the cores as they orbit into the ICM.

3.3 Final relaxation

The pressure waves keep on extending out of the frame shown on the maps. Their integrity is already broken at $z = 0.12$ but some features persist down to the present day. To the opposite, the cold fronts remain fairly stationary and stable on the temperature maps until $z = 0.03$ and only weaken by $z = 0$. The cold fronts survive the shock preceding them, not only because they stall in their outward propagation, but also because they do not start to “wash out” in temperature maps as the shocks do in our simulation on the $z = 0.12$ and $z = 0.10$ maps, even they it can still be tracked later on to larger radii. Therefore, if major mergers are the main cause of cold fronts, their smaller duty cycle will make the bow shocks they are associated with intrinsically more difficult to detect in X-ray temperature maps.

In the meantime, the sub-clump cores merge as they reach their second close encounter: while the pressure maps in Fig. 6 track the final inspiralling and merging, the entropy maps of Fig. 7 show a more complicated behaviour. In addition to the final merging, they show two streams linking the central region to the top right cold front, which develop between $z = 0.06$ and $z = 0.03$.

We stress here that the temperature and Compton y parameter maps of Figs. 5 and 6 have been obtained on a 500 kpc thick slice containing the orbits of the two subcluster cores. This has allowed us to achieve high spatial resolution and to precisely visualise interesting features. In reality, limited resolution and projection effects will degrade the maps. Recent observations have improved by large factors in resolution (*Chandra* reaches $1''$, corresponding to a comoving size of $4.6 h^{-1}$ kpc at $z = 0.3$), but projection effects may still significantly smooth and distort details like those shown on our maps. Features which are prominent and asymmetric with respect to the cluster centre like cold fronts may be the least affected, but thin patterns more symmetric with respect to the cluster centre and extending over a larger area such as shocks may significantly suffer from projection. Note also that because X-ray emission is concentrated at the cluster centre, observations of temperatures variations which are weak and/or with small spatial extent far from the centre present a major challenge.

3.4 An X-ray picture of the ICM

Some of the physical processes mentioned above are directly echoed in X-ray observations of the ICM. Figure 8 gives the X-ray surface brightness S_X at four different times, over the same, 500 kpc-thick region that was used for Figs. 5 to 7. The panels show a variety of morphologies.

The top left panel shows two spherical, clearly separated

subcluster cores at $z = 0.24$ (in white), before their first close encounter. At $z = 0.18$ (top right panel), as they orbit towards their apocentres, the two cores begin to lose a fraction of their gas in their wake, seen as diffuse white emission, and the transition from red to black in the lower left and upper right parts of the image becomes sharper, a direct consequence of the merging shock propagating outwards. The resemblance of this panel with some of the *Chandra* pictures discussed by Markevitch et al. (2002a) or Markevitch et al. (2000) is striking. At $z = 0.12$ (bottom left panel) the cores contract, acquire an elongated shape, and fall back in the central potential well, while the external pressure wave progresses towards the outer layers of the cluster. The bottom right panel ($z = 0$) shows what seems a fairly relaxed cluster, but with the clear luminosity gradient of the cold front of the bottom left region.

Again, note that projection effects may blur features in the X-ray luminosity which are clearly seen when using a 500 kpc-thick slice cutting through the cluster centre. In fact, X-ray emission is much more compact and peaked than, for instance, the Sunyaev-Zeldovich effect measuring the Compton y parameter. This becomes obvious when comparing Fig. 8 to Fig. 6 at $z = 0.18$. In the former, the diameter of the inner “structure”, taken at a factor 100 down from the peak of the emission, does not exceed ~ 2 Mpc while the high-pressure zone, at the same dynamic range from the peak value, reaches more than 4 Mpc on the $z = 0.14$ slice of Fig. 6. As a result, the smoothing due to projection will be much reduced in X-ray luminosity maps in comparison to pressure maps.

4 RESOLVING SHOCKS IN THE ICM

We have only considered one global shock in the previous section, although complex multiple shocks in the ICM are expected to develop during mergers. In fact, the substantial density of the core of our merging subclusters, together with their high infalling velocity results in a variety of supersonic features. According to common lore, SPH simulations only provide limited shock front resolution. Here, however, the high resolution of the simulation enables us to partly circumvent this restriction and to bring out two aspects of shock propagation that we find particularly striking. We first focus on the $z = 0.20$ and $z = 0.18$ snapshots, when the bow shock or its pressure wave catch up with the merger shock. Then, we briefly discuss the possibility of secondary shocks.

4.1 Merger and bow shocks

First, we discuss the primary quantities temperature and pressure profiles across the shock and cold front selected at $z = 0.14$. Then, we consider the velocity field and entropy evolution as secondary probes.

4.1.1 Temperature and pressure profiles

The broad geometry and sequence of temperature variations remain simple and seem to confirm the picture sketched by Markevitch et al. (2000): merger shocks first form in a slab separating the two subcluster cores and normal to the direction of merging as the regions of the gas surrounding

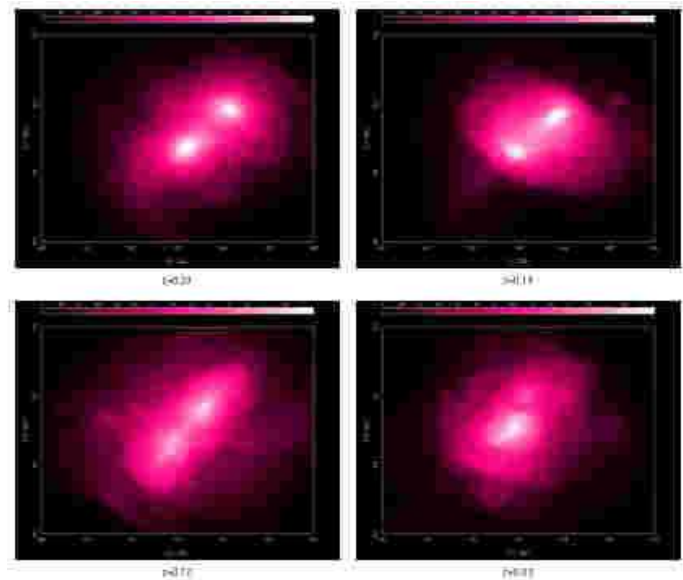


Figure 8. X-ray bolometric surface brightness S_X (arbitrary normalisation) at four different stages after z_{merg} . S_X is colour-coded logarithmically and has been integrated over a 500 kpc-thick slice. The region shown is the same as in Fig. 5, and the colour scale is the same for the four images. Note that the upper right picture is strikingly similar to some of the *Chandra* images in Markevitch et al. (2000 2002a), as is the sharp transition between red and black to the lower left of the $z = 0.03$ panel, due to the cold front. In reality, projection effects may degrade the sharpness of the weak features, but the strongest contrasts between white and orange colours will remain unaffected (see text for discussion). A better, high resolution version of this figure is available at: <http://www-astro.physics.ox.ac.uk/~hxm/ColdFronts/>.

the subclusters situated in front of each of them penetrate one another at supersonic velocities. These merger shocks propagate outwards as pressure waves in the ICM once the motion of the subcluster gas in which they originate has slowed down or when the merger shocks have swept up all the subcluster gas and are situated at the interface between the shock heated subcluster gas and the relatively more stationary ICM with lower opposite velocity. Bow shocks, on the other hand, are due to the supersonic (transonic here) motion of the dense gas cores CG_1 and CG_2 of the subclusters inside the newly formed ICM. The ICM includes contribution from the subcluster gas surrounding the dense cores which has been stripped off by the merger shocks. As bow shocks can propagate out in the ICM faster than the merger shocks or their associated pressure wave if the out-bound clump velocity remains sufficient, they can eventually merge with the latter. The complexity of the symmetric high-temperature regions in Fig. 5 (see $z = 0.18$) suggests that this is the case in our simulation.

The left and right top panels of Fig. 9 show the temperature profiles across the lower left shocks at $z = 0.20$ and $z = 0.18$ respectively, while the left and right bottom panels give the Compton y parameter profiles at the same redshifts. The profiles show the projected quantities along a test segment reaching from the unaffected ICM (at the exterior of the outermost shock front) in the bottom left region of the above Figures 5 to 7 to deep in the core region of the newly formed cluster. This line probes the highest temper-

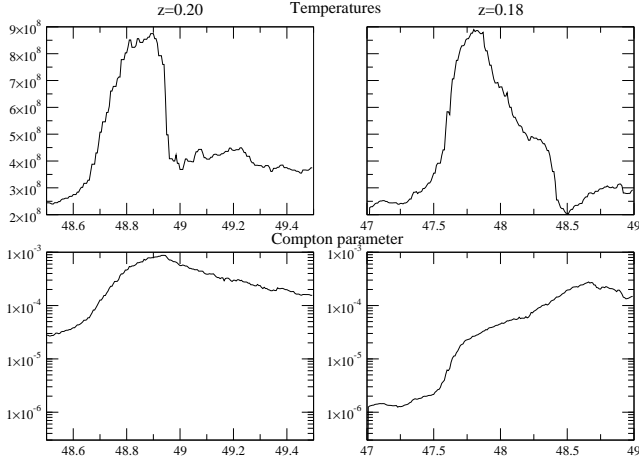


Figure 9. Temperature and Compton y parameter projected over a 500 kpc thick slice in z , computed along a test line cutting through the lower left bow shock in the x - y plane, at $z = 0.2$ and $z = 0.18$ (see text for details on the choice of the test line). The abscissa shows the y -coordinate. The upstream region of the shock is to the left of the temperature and pressure rise. While the cold subcluster clump is not visible on the $z = 0.2$ temperature cut, its extension is evident at $y = 48.5$ on the $z = 0.18$ temperature cut.

ature zones (in blue) of the lower left shocks at $z = 0.2$ and $z = 0.18$. Note that because these temperature extrema are drifting in the x - y plane, we have taken the test line parallel to the y -axis with the $z = 0.20$ lower and upper end points at (43.1, 48.5) and (43.1, 49.5) Mpc and the $z = 0.18$ lower and upper end points at (43.1, 47) and (43.1, 49) Mpc. The abscissa of Fig. 9 is labelled in the global y -coordinate of the simulation (in Mpc). This test line setup allows us to capture all the above features on a straight line. We note that since the test line is not strictly parallel to the direction of propagation of the shock, this offset will dilate the scale. A stricter result would be obtained using a moving test line so that it remains aligned with the direction of propagation of the shock, but we would not gain much more information.

At $z = 0.20$, the sub-clumps have gone slightly past their first closest encounter (see the top right panel of Fig. 4). The bulk of the CG_2 particles reach $y = 48.5$ at $x = 43.1$, but the temperature and pressure rise characterising the shock are clearly seen at $y \sim 48.7$. Between $y = 48.65$ and $y = 48.8$, the temperature rises by a factor of $T_2/T_1 \sim 2.7$ while the pressure rises by a factor $P_2/P_1 \sim 10$, where indices 1 and 2 respectively label the upstream and downstream regions. Assuming a flow normal to the shock, the Rankine-Hugoniot relations give a high upstream Mach number $M_1 \sim 2.6$ to 2.8. We will show in paragraph 4.2.1 below that this value is too high and that the upstream velocity of the flow with respect to the shock is of order 2000 km s⁻¹ only: the flow is transonic/slightly supersonic. (If the flow is significantly oblique to the high temperature front, it may be subsonic, without shock). Because of this uncertainty, we use the entropy evolution in paragraph 4.2.2 to verify that a shock actually develops.

As we have already stressed in the previous section, it is difficult to estimate how the merger shock, due to the initial compression of the ICM gas intervening between the subcluster cores during their first approach, or its remnant

adds to the effect of the bow shock induced in the direction of motion of the subcluster cores after their first close encounter as the steep rise singled out on the temperature and Compton y profiles at $z = 0.20$ is generated. In fact, both types of shocks may result in features similar to the ones we observe. Clearly separating these two components would require a full 3D analysis and even higher spatial and temporal resolution.

In the downstream region corresponding to the central zone of the newly formed cluster, the temperature of the gas heated by both shock and compression decreases as a result of the adiabatic expansion of the gas in the wake of the shocks; this is due to the divergent motion of the flow as it follows CG_1 and CG_2 . Note that at $z = 0.20$ the temperature T_2 of the flow is fairly constant over the range $y = 49$ to $y = 49.5$. The pressure P_2 declines monotonically by a factor of 5 from the peak at $y = 49$ all the way to $y = 49.5$.

Later, at $z = 0.18$, as the sub-clump cores are already 1.5 Mpc apart in the x - y plane and on their way to their apocentre, they can be viewed as two pistons compressing the gas in front of them. Because their motion is not supersonic anymore in a 2×10^8 K hot ICM, they will not sustain the shock. As a result, it transforms into a pressure wave propagating upstream. The upper right panel of Fig. 9 indicates that the wave is some 750 kpc ahead of CG_2 , at $y = 47.6$, with the outskirts of the cool core of dense gas clearly visible at $y = 48.5$ on the temperature profile. This is confirmed by comparison to the $z = 0.18$ snapshot of Fig 7.

Note that no such temperature drop was visible on the $z = 0.20$ map simply because both CG_1 and CG_2 are then slightly out of the 500 kpc thick slice used to compute the profiles. The amplitudes of the jumps in both pressure and density are similar at $z = 0.20$ and $z = 0.18$, but the shapes of the profiles differ in the downstream region, a possible consequence of the readjustment of gas and dark matter density profiles in the central region of the cluster.

4.2 Velocity and entropy across the shock

4.2.1 Gas velocity

Fig. 10 shows the projected gas velocity field at $z = 0.2$ of a square slice of width 2 Mpc and thickness 500 kpc spanning over the lower left shock region, overlaid on the colour-coded emission-weighted temperature map selected from the same slice. Note that to best cover the temperatures ranges in the selected areas shown here and in Fig. 11, the temperature colour scales are different in Figs. 10 and 11, and that they also differ from the scale of Fig. 5.

The velocities have been computed in the rest-frame of the simulation, and the longest arrows correspond to 1000 km/s. While the ICM outside of the bow shock (to the lower left) is accreting towards the cluster centre, the amplitude of the velocity of the gas strongly decreases as it hits the strong positive temperature gradient, for example over the thin yellow line passing over $(x,y)=(43.25, 48.5)$, as expected for a shock. In the post-shock, downstream region, on the upper right side of the temperature gradient, the motion of the shocked gas is either negligible with the scales plotted (43.75, 48.5) or directed outwards of the cluster centre if it

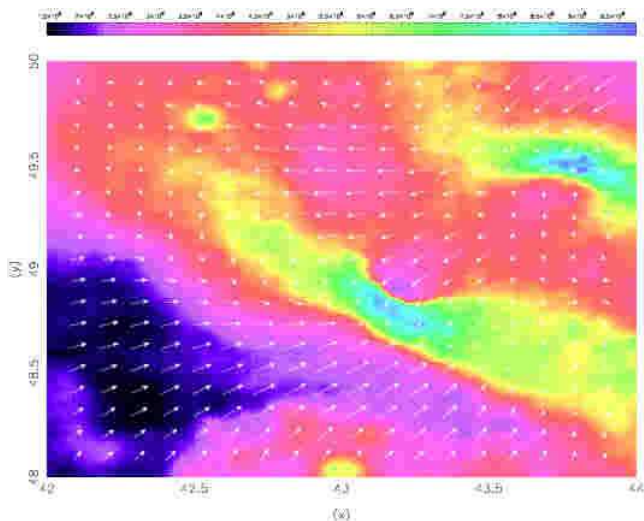


Figure 10. The $z = 0.2$ projected gas velocity field in a 500 kpc thick, 2 Mpc wide slice cut in the x - y plane around the lower left cold gas core. The background shows the emission-weighted temperature map (colour-coded linearly with a scale particular to this Figure). The largest arrows correspond to a velocity of $\sim 1000 \text{ km s}^{-1}$. Note the discontinuity of the velocity field over the shock (for instance, $x = 43.25$, $y = 48.5$). A better, high resolution version of this figure is available at: <http://www-astro.physics.ox.ac.uk/~hxm/ColdFronts/>.

is on the subcluster core or in its wake. Note that in the rest frame of the shock, both upstream and downstream gas would have inward velocities.

Fig. 11 is the $z = 0.18$ version of Fig. 10, computed over a thin slice with the same geometry. Here, while the x -range has been kept similar as in Fig. 10, the y -range has been shifted downwards by 1 Mpc to follow the propagation of the shock. The same features are apparent, except the velocity-reversing region at the shock which has dilated in size along the direction of the propagation of the shock. The upstream accretion velocity field is weaker than at $z = 0.20$, a possible consequence of the region being farther from the cluster centre. The lower left cold gas core can be seen as the lower temperature zone at $(43, 48.5)$ (remember that the colour scale is not the same as for Fig. 10). The extended shape of the cold gas core suggests that a phenomenon such as adiabatic expansion of gas particles heated at core passage begins to develop. The whole cold feature still moves coherently with the surrounding flow, as does its wake, down to the 80 kpc resolution mesh on which we computed the velocity field. This resolution is sufficient for our purposes as we describe the motions of extended features in the ICM but would be too low to draw conclusions on changes in the direction and amplitude of the velocity field at the boundary of this cold feature as possible precursor of the cold front. Given these precautions, the direction of the flow in the zone between the cold zone and the shock then slightly rotates to align with the y -axis at $x = 43$ and $y = 48.25$, while remaining at significant amplitude. At later times when the cold front has developed, we have also checked that no velocity discontinuity is apparent on maps of gas velocity similar to Figs. 10 and Figs. 11, at the interface between the cold front and its surrounding ICM.

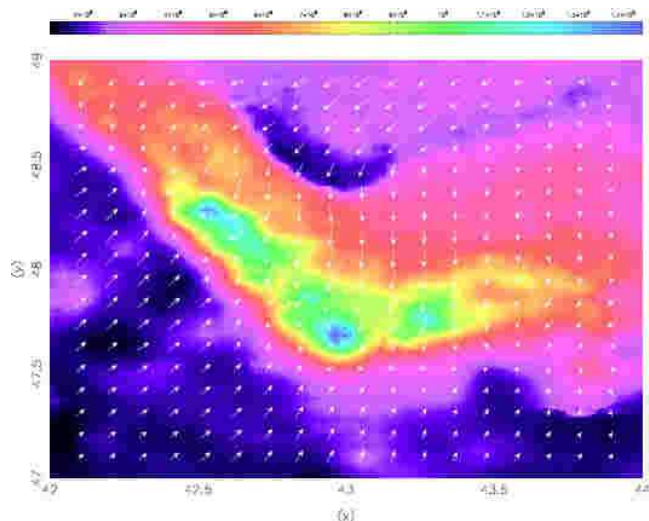


Figure 11. Same as Fig. 10, but at $z = 0.18$ and with a different colour scale for the temperature. The region shown has been translated downwards from Fig. 10 by 1 Mpc, to better follow the shocks. A better, high resolution version of this figure is available at: <http://www-astro.physics.ox.ac.uk/~hxm/ColdFronts/>.

4.2.2 Entropy variation

The entropy variation due to a single shock or even a series of shocks is too small to be read directly in Fig. 7, with Mach numbers $M \lesssim 3$ as typically found for sub-clumps orbiting in the ICM. Therefore, we follow the approach of Keshet et al. (2003) who trace shocks in an SPH simulation of the intergalactic medium, and gather the evolution of the entropy of a set of gas particles. Not only can this method confirm that the large temperature and pressure gradients discussed in Section 4.1.1 are associated with a shock, but it could also be used in higher resolution simulations to separate out consecutive shocks, depending on the initial set of Lagrangian particles chosen.

At $z = 0.28$, shortly after the merger, we select all gas particles in the lower left zone of the ICM, with $(x, y, z) \in ([42, 42.5], [47, 48], [48.5, 49.5])$ Mpc. We find about 1100 such particles; they are then tracked as they move in the ICM. This Lagrangian region trails the subcluster core CG_1 (see the lower left panel of Fig. 4) and it is initially unaffected by the shock. The possible merger shock that would develop upstream of the subcluster core before first passage as a result of the compression of the intervening gas is expected to have little impact on this trailing set of particles, in contrast to the later bow shock. In fact, the set of selected particles is right in the direction of propagation where the bow shock seems the strongest on the $z = 0.18$ map of Fig. 5.

Figure 12 gives the entropy evolution Δs_* of this gas, with $s_* = \log(T/\rho^{2/3})$. The black, red and green curves respectively give the 10, 50 and 90% quartiles of the distribution. We distinguish two features. First, there is synchronous increase in s_* for all particles in $0.2 < z < 0.16$, although the degree of variation in s_* differs: it is less than 0.05 (Mach number $M_1 = v_{\text{shock}}/c_{s, \text{upstr}} = 1.5$) for the 10 first percent of the particles and more than 0.2 ($M_1 = 2$) for the last 10 percent. We have checked that virtually no selected gas particle is left unaffected. Second, when the shock has passed the test Lagrangian region (at $z \lesssim 0.15$), the entropy per

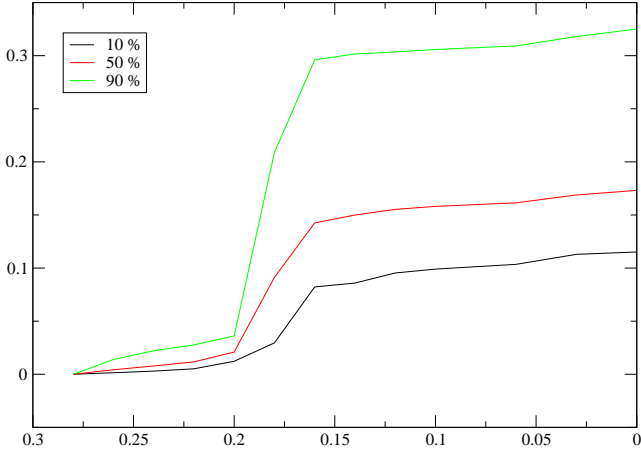


Figure 12. The evolution Δs_* of the entropy of gas particles selected shortly after the merger. The Lagrangian region chosen is a 0.5 Mpc^3 zone close to the lower left of the ICM (trailing CG_1 before first core passage), which is only affected by the bow shock at $z \sim 0.18$. We define $s_* = \log(T/\rho^{2/3})$ and show the 10, 50 and 90% quartiles of the distribution of Δs_* (black, red and green curves respectively). Note the characteristic synchronous entropy increase between $z = 0.2$ and $z = 0.18$ due to the shock, together with the spread in Δs_* by more than a factor of 5 between the first and last 10 percents of the distribution.

particle changes little down to $z = 0$. To be concise, and because our goal is to clarify the nature of the temperature gradient apparent on the $z = 0.18$ maps, we have restricted ourselves to only one set of particles of the ICM.

To conclude this paragraph, it is important to note that no gas particle of CG_1 nor of CG_2 is closely trailing the bow shock (see Fig. 4), showing that such shocks are only formed because of the original internal pressure of the two clumps and because of their supersonic velocities (the typical “piston” picture) and do not convey any elements of the clumps in their vicinity.

4.3 Secondary merger and bow shocks

Fig. 5 also shows the presence, after $z = 0.1$, of temperature gradients of smaller size at the centre of the cluster. These secondary features, probably “merger” shocks in the classification of Markevitch et al. (2000), form in a process which is a scaled-down repeat of the initial compression of the ICM gas situated between the cold dense subcluster cores which took place before their first encounter discussed in paragraph 3.1. At $z = 0.1$, Fig. 4 shows that both CDM_1 and CDM_2 have an extended shape compared to their $z = 0.28$ geometry. The densest parts of the clumps, however, have almost reached their second encounter in the x-y projection. An interesting side effect besides the temperature rise in the centre of the $z = 0.1$ panel of Fig. 5 is the thin tail of cold gas leaking from both cold fronts. It is particularly visible above the lower left front, and forms in the wake of the densest part of CG_2 as it falls back towards the cluster centre.

At $z = 0.1$, the secondary shocks are confined to the very central region by the convergent gas flows surrounding CG_1 and CG_2 , as they move towards their second close encounter, so that their extension is impeded in the direction of the cold front. They can, however, extend in the NW-

SE direction of the map. As the dense cores go past their second close encounter this coherent flow stops and the secondary shocks are released. At this point, they may be more accurately described as “bow” shocks as the piston effect of CG_1 and CG_2 takes place again. The secondary shocks clearly extend on at $z = 0.06$ just before collapsing again to the centre at $z = 0.03$.

Although Nagai & Kravtsov (2003) state that their bow shocks heat and disrupt their cold front, it is not clear that this happens here: the secondary bow shocks seem to only affect the low temperature tail of the cold fronts which is pointing to the cluster centre, but for instance the upper right cold front itself seems largely unaffected by these secondary features. Mixing or diffusion of the cool phase into the hot ICM may explain the final disruption of the cold fronts.

5 CHARACTERISING THE COLD FRONTS

Similarly to what we have previously done for shocks, we first demonstrate that the features seen in the temperature maps at $z \lesssim 0.16$ are cold fronts, we then select the particles of the lower left cold front and trace them back to elucidate their possible origin.

5.1 Physical attributes

Figures 13 and 14 respectively give the Compton y parameter, in arbitrary units, and temperature profiles computed at $z = 0.1$ on a test line cutting through approximatively the longest extension of both cold fronts and through the centre of the cluster. The profiles have been computed from the values projected over a 500 kpc thick slab normal to the line of sight (z -direction). The label of the abscissa has an arbitrary origin. The pressure profile, on one hand, rises to the centre of the cluster, is smooth on both sides, and there is no discontinuity over the expected location of the cold fronts. The complex features at the centre can be due to the presence of high pressure particles which have been stripped off the sub-clump cores, of the secondary compression of the intervening gas, or of the birth of secondary bow shocks. On the other hand, the temperature profile is symmetric but discontinuous. The temperature rises in the centre and on the outskirts of the test line, but drops by a factor 4 to 6 in $1 < x_{\text{loc}} < 2$ and $3.5 < x_{\text{loc}} < 5$ Mpc with respect to the outer temperature value. The exterior discontinuity corresponds to the envelope of the cold fronts. At $z = 0.1$, CG_1 and CG_2 are ~ 1 Mpc apart. While the interior temperature discontinuity at $x_{\text{loc}} = 2$ Mpc is sharp and goes over CG_2 , CG_1 is slightly out of the slice resulting in a smoother interior temperature discontinuity at $x_{\text{loc}} = 3.5$ Mpc. Assuming that pressure equilibrium has been achieved between the interior of the cold front and the surrounding ICM, the factor 3 to 4 drop in local temperature yields a factor 3 to 4 increase in the density of gas of the cold front compared to that of the ICM.

Both cold fronts form behind the bow shocks induced by the motion of the cores. While the ICM gas downstream the strong shocks cools down as it expands adiabatically, we show in the next paragraph that it cannot be responsible for

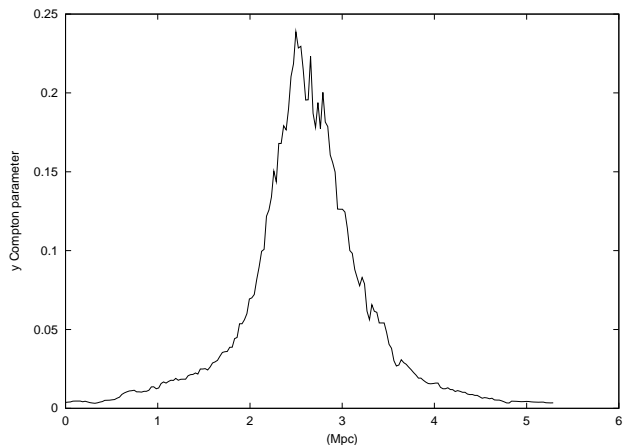


Figure 13. Profile of the Compton y parameter of the cluster over a test line passing through the cold fronts, in arbitrary units. The profile has been computed from the value projected over a 500 kpc thick slab normal to the z -direction at $z = 0.10$, and the test line cuts through the centre of the cluster. The label of the abscissa has an origin chosen so that the cluster centre is at ~ 2.5 Mpc. Note that the pressure rise to the centre of the cluster is smooth on both sides, and the late-time signature of the merging/bow shocks has reached beyond the ranges shown here. The complex features seen at 2.5 Mpc may be due to the combination of the remains of the cold, high pressure merging sub-clumps and the secondary bow shocks.

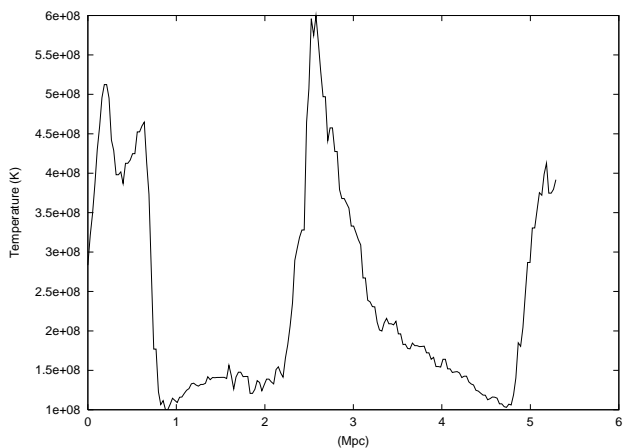


Figure 14. Same cut as in Fig. 13, but for the temperature profile of the gas. Note the globally symmetric shape: the gas temperature rises to the left, central and right regions ($x_{loc} < 1$ Mpc, $2 < x_{loc} < 3$ Mpc, and $x_{loc} > 5$ Mpc). Between these zones, the signature of the cold fronts and of the wake trailing the subcluster cores is striking, as they extend over more than 1 Mpc along the direction shown. The upper right cold front of the ICM is on the right.

the formation of cold fronts: the particles constituting the fronts have a clear-cut origin.

5.2 Tracing the origin of the cold fronts

We use again the Lagrangian description of the fluid to trace back the particles of the cold fronts. We set up a method to select SPH particles in the simulation directly from both

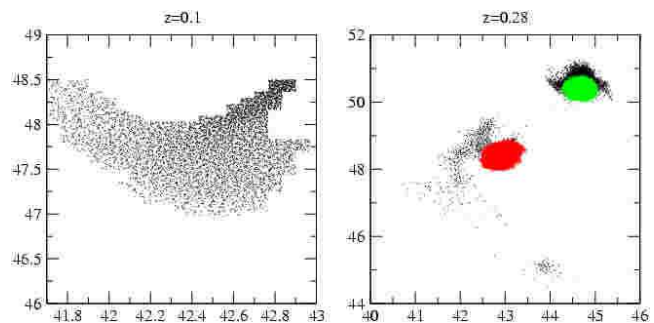


Figure 15. Tracing of the gas particles of the lower left cold front. Left panel: position in the x - y plane of the particles of the cold front. The particles have been chosen below an appropriate threshold in the temperature maps at $z = 0.10$. Right panel: same particles once they have been traced back to $z = 0.28$. The particles of the two cores CG_1 and CG_2 are also shown in red and green respectively. Note the overlap between CG_2 and the initial position of most of the particles of the cold front. A better, high resolution version of this figure is available at: <http://www-astro.physics.ox.ac.uk/~hxm/ColdFronts/>.

spatial criteria and from a threshold applied to the fields shown in the maps of Fig. 5 to Fig. 7. We can combine selection masks along different directions in the case the target is conveniently expressed as an intersection.

To select the cold fronts, we combine two cuts in two projected, emission-weighted temperature maps along two orthogonal lines-of-sights through the cluster. Particles of the cold fronts are selected at $z = 0.1$ when the cold fronts are well developed. We then trace them back to shortly after z_{merg} and find that almost all of them originate from the two subcluster cores: gas particles from the lower left cold front come from CG_2 while those from the upper right cold front come from CG_1 . Fig 15 shows the origin of the particles selected in this way in the region of the lower left cold front, with the particles inside the mask shown on the left panel: their position at $z = 0.28$ is given in black in the right panel, and CG_1 and CG_2 are overlotted in red and green, respectively. Note the clear overlap between the particles traced back from the mask and those of CG_2 , supporting that the bulk of the mass of the lower left cold front originates in CG_2 . There is small additional contribution to the mass of the cold front from gas particles which originally surround CG_1 at its upper left, and from a few “fuzzy” particles of the $z = 0.28$ ICM.

Conversely, if we follow the forward evolution of CG_1 and CG_2 from z_{merg} , we find that the envelope of the position of the outer particles of both clumps at $z = 0.1$ corresponds well with the location of the cold fronts, while their inner densest part has already fallen in the central region of the cluster. This is seen by comparing the location of the red clump of the lower left panel of Fig. 4 with the left panel of Fig. 15. Apart from the cold front zone, neither CG_1 nor CG_2 loose particles to the surrounding ICM. Because the evolution is qualitatively very similar for the upper and lower cold front, we will exclusively deal with the upper cold front (associated to CG_1) in the rest of this study.

We show in the next section that the particles of CG_1 constituting the cold front are expelled from the dark matter potential well, while other surrounding and trailing

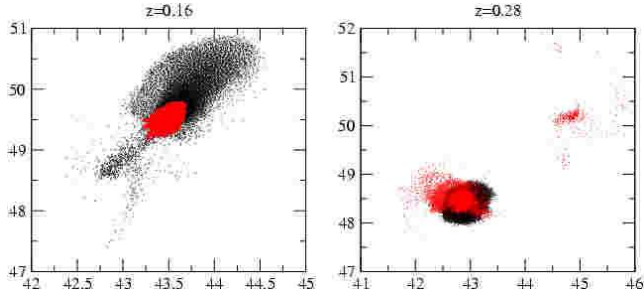


Figure 16. Tracing of the high pressure gas particles of the upper right cold front region. Left panel: projection in the x-y plane of the $z = 0.16$ positions of the particles selected at $z = 0.1$ by their high Compton y parameter (in red) in a 3×4 Mpc region encompassing CG_1 : these particles map the bottom of the local gravitational potential well. The $z = 0.16$ positions of the particles of CG_1 are repeated in black: note on one side of the potential well the extended plume up to $y \sim 51$ and $x \sim 44.5$ Mpc which constitutes the exterior envelope of the cold front, on the other side a set of particles falling back or trailing. Right panel: corresponding positions of the two sets of particles at $z = 0.28$. While a fair fraction of the red particle overlaps with CG_1 at $z = 0.28$, some surrounding particles, and some particles of the lower left of CG_2 also end up with high pressure in the CDM_1 potential well at $z = 0.1$. A better, high resolution version of this figure is available at: <http://www-astro.physics.ox.ac.uk/~hxm/ColdFronts/>.

gas particles simultaneously fall in the local potential well. Information about the origin of these latter gas particles is obtained if we select the particles at $z = 0.1$ in the upper cold front region with the highest Compton y parameter. The left panel of Fig. 16 compares the spatial distribution at the epoch of formation of the cold front ($z \sim 0.16$) of particles selected according to their y parameter only, in red, with the positions of particles of CG_1 (in black). The right panel traces back both ensembles to shortly after z_{merg} . While the particles with highest pressure at $z = 0.1$ trace as expected the minimum of the potential well, they do not map back exactly onto CG_1 : a number of particles also stem from its surroundings and from the outskirts region of CG_2 . We will see in the next section how an energetic analysis of the black and red particle ensembles of Fig. 16 gives insight into the process at work.

To summarise, the particles of the cold fronts are essentially composed of the particles of the cores of the two sub-clumps. Cold front particles evolve as a bulk from the epoch of formation of the front until the end of the simulation. Interestingly, the gas particles located at the bottom of the local gravitational potential associated with the CDM_1 / CDM_2 substructures do not only originate in the cores of the merging clusters but also in their initial outskirts at z_{merg} .

6 A PHYSICAL EXPLANATION FOR THE FORMATION OF COLD FRONTS DURING MERGERS

To synthesise the description of the previous sections and understand in detail the mechanism responsible for the formation of the simulated cold fronts, we employ an energetic approach. The variables U , W , K and T respectively stand

for the internal, potential, kinetic and total energy of a particle. U and K are directly obtained from the simulation data, while W is obtained from the contribution of the DM particles of the cluster only. We neglect the contribution to W from the gas particles, from the large scale structure, and from the cosmological constant. We first discuss the energy evolution of the CG_1 as a whole from z_{merg} down to the present. We then focus on the epoch of formation of the cold front. We finally compare to other work.

6.1 Global energetic evolution of CG_1

Figure 17 gives the evolution of the distribution of the total energy $T = U + W + K$ of the gas particles (of mass $1.3 \times 10^8 M_\odot$ each) of CG_1 . The upper, middle and lower curves correspond to the 10, 50 and 90 percent quartiles of the distribution of the particles. In practice however, we always have $K < U < |W|$ for almost all particles, and the time evolution of the sum $\sum T$ of the total energies of all the particles of CG_1 is mainly driven by that of $\sum W$.

In the first stage from z_{merg} down to $z = 0.2$, the sub-clump core moves towards the centre of the newly formed cluster. The total energies T decrease with the gravitational potential energy and are not compensated by sufficiently symmetric increase in kinetic energy: mostly confined in their local gravitational well, particles of CG_1 head towards the cluster centre where the proximity of CDM_2 decreases W . In the next stage from $z = 0.2$ to $z = 0.1$, T globally increases as CG_1 moves towards its apocentre. Finally, from $z = 0.1$ to $z = 0$, T decreases again as the cores eventually merge. Note that the scatter increases continuously from $z \sim 0.15$ down to $z = 0$: this corresponds to the release of the cold front, which remains stable and does not fall back towards the cluster centre with the core of CG_1 .

Figure 18 confirms this as it separates the gravitational potential W and internal energy U of the particles of CG_1 (left and right panels respectively). While the evolution of the distribution of the gravitational potential is qualitatively the same as that of T , the evolution of the internal energy shows that the gas is promptly heated up by compression as the gravitational potential decreases around $z = 0.2$, part of the gas then cools down as a signature of the cold front until $z \sim 0.1$. The densest, hottest particles of CG_1 at $z \sim 0.1$ are heated up again during the final inspiralling stage, as shown by the gradient in the 90 percent quartile green curve at $z \lesssim 0.1$. The cold front starts developing at $z \sim 0.15$, where the width of the distribution of the gravitational energy W of the particles begins to increase down to $z = 0$ (see the left panel of Fig. 18). In fact, gradients in the evolution of the distribution of the gravitational energy of the gas particles of CG_1 are fairly symmetric in the range $z = 0.25$ to $z = 0.15$ with respect to $z = 0.2$, suggesting that stripping of the dark matter clump is not dominant. To the opposite, gradients in the evolution of the distribution of the internal energy of the gas particles of CG_1 are asymmetric: the profiles change in the epochs $0.2 \gtrsim z \gtrsim 0.15$ with respect to their pre-encounter evolution. Heating/cooling processes are not symmetric with respect to core passage. Particles have been heated up at core passage by compression or by possible merging shocks if their density is sufficiently low. As the subclump moves on the outward path of its orbit, particles of CG_1 whose binding energies in the potential

well of CDM_1 are minimal will (1) tend to expand and cool down and (2) more easily decouple from the motion of CDM_1 .

Between $z = 0.2$ and $z = 0.15$, the “cooling rate” as given by the gradient of the 10 percent quartile of the particle distribution (black line in the right panel of Fig. 18) is pronounced. Caution is necessary here, given that we simply plot the quartiles of the distribution at successive times: for instance, the coolest particles of the distribution at $z = 0.15$ can of course be the hottest at $z = 0.2$ and conversely. After $z = 0.1$, the black line (10 percent of the distribution) levels off at $\sim 2 \times 10^{58}$ erg, unlike the red and green lines which show an increase in internal energy at $z \lesssim 0.12$. The cold front, made of dense particles which are expelled out of the local gravitational potential and further cool adiabatically, makes a large fraction of the 10 percent particles with internal energy below $\sim 2 \times 10^{58}$ erg. The additional contribution is from particles trailing CDM_1 and leaking to the centre of the cluster.

To properly explain the origin of the cold front during mergers requires to understand how a fraction of the CG_1 particles are able to climb up the local gravitational potential.

6.2 Formation of the cold front

On Figure 19, we plot in red the positions of each particle of CG_1 in the gravitational potential W , while the black set gives the positions of the pressure-selected particles of CG_1 which will have fallen in the potential well of CDM_1 (see 5.2) by $z = 0.1$. As the red set has been overplotted, it can hide black particles. Note also that when a particle belongs to both sets, it appears in red. The positions shown in abscissa correspond to the y-axis of the simulation. The right and left panels correspond to $z = 0.16$ and $z = 0.12$ respectively. Recall that CDM_1 reaches its apocentre at $z \sim 0.15$ (see the middle panel of Fig. 2). We first describe the two panels in turn and then propose an explanation.

At $z = 0.16$, the distribution of the core set ($y > 49$ Mpc) of the CG_1 particles becomes asymmetric in the gravitational potential which is mostly generated by the particles of CDM_1 . We have checked that this asymmetry is not present (to this level) at a previous epoch and that it starts developing at this point. At $y \lesssim 48.6$, in the wake of the gravitational potential of CDM_1 centred at $y = 49.7$, a second, slightly smaller potential well, which at $z = 0.16$ is not yet clearly mapped by particles, starts to be filled up with particles of CG_1 . This second potential well is generated by CDM_2 and captures some of the gas particles of CG_1 which have been stripped off by tidal forces and/or ram pressure. These two processes would take place when, respectively CDM_2 is sufficiently close to CG_1 and when its velocity in the surrounding ICM is high enough. Note that a fraction of the black particles have not yet fallen in the local potential well of CDM_1 , even if they stay spatially close to it (see the red particles in the left panel of Fig. 16 for another projection). This fraction also corresponds to red particles surrounding CG_1 in the right panel of Fig. 16.

At $z = 0.12$, the cold front is already well developed on the temperature maps (Fig. 5), and CDM_1 has begun its retrograde motion along y . The distribution of the CG_1 particles in the local gravitational potential is now highly

asymmetric (see the left panel of Fig. 19), extending from its minimum at $y = 49.5$ to $y \simeq 51$. Particles in the range $50.2 < y < 51$ are responsible for the upper right cold front in the maps. Two other features are striking. First, most of the trailing red particles stripped off from CG_1 have now fallen back in the potential well of the second halo. Second, the black particles have moved close to their selection location as they accreted in the bottom of the CDM_1 potential well, where they are compressed and sustain the equilibrium with the particles of CG_1 forming the asymmetric profile: the pressure selection of gas particles in paragraph 5.2 has been done at slightly later $z = 0.1$. In short, we find that the centres of mass of CG_1 and CDM_1 move together after first passage during most of the outward part of their orbit, but that a phase shift is introduced as CDM_1 reaches its apocentre: the inward motion of CG_1 is delayed. Similar conclusions have been foreseen by Roettiger et al. (1997) and stressed by Ricker & Sarazin (2001) (see their paragraph 3.2). We now suggest a qualitative picture which accounts for the formation of the cold fronts in our simulation.

The effect of the surrounding ICM pressure, present all along the inspiralling of the subcluster core, has strong consequences when CDM_1 reaches the apocentre. In the following qualitative discussion, we will first not consider the global pressure gradient of the newly formed cluster, to simplify the picture: we assume a uniform ICM pressure. Note that this hypothesis is a better approximation at the apocentres of the orbits of the subclumps, where our cold fronts are generated, than at the inner parts of the cluster (see Fig. 13, where the centre of the cluster is at $x \sim 2.5$). We further assume that the flow is incompressible, which is valid at the outskirts of the orbit where motions are subsonic. Before apocentre passage, CG_1 stays in phase with CDM_1 at least from the time of central passage: the offset between the two centres of mass is always less than 100 kpc (see Fig. 2). Recall here that first passage of the two subcluster cores occurs at $z \sim 0.22$. Comparing the red lines (dark matter) in the upper left (x-coordinate) and middle (y-coordinate) panels of Fig. 2 between $z = 0.22$ and $z = 0.16$ (the epoch of maximal x and y extension) shows that this part of the orbit of CDM_1 is inclined to ~ 60 degrees anticlockwise in the x-y plane.

After first core passage, the gravitational force acting on CDM_1 and CG_1 is central, and is due to the global smooth cluster potential and to the sub-clump 2. However, the total force seen by the gas of CG_1 also includes an “inertial” pressure force induced by its accelerated motion, which acts in the same direction, but with opposite sign. This is true even if the surrounding ICM pressure is uniform. (We will employ acceleration here in its vectorial sense.) Because total forces acting on CG_1 and CDM_1 differ, this will lead to a decoupling of the part of the gas clump (the less bound particles) from the dark matter clump. This decoupling of the part of the gas clump in turn, is reduced by the gravitational pull introduced by CDM_1 as the two components of the sub-clump do not anymore share the same spatial distribution.

Because pressure gradients induced by the accelerated motion of CG_1 act opposite to the overall gravitational pull, they tend to eject gas outside of the local gravitational potential. This liberation of gas is in the outward direction with respect to the centre of the cluster. It has little effect before

apocentre passage because gas particles pushed forward in the direction of motion by this force may immediately fall back in the local gravitational potential of the dark matter subclump, whose eccentric orbit make it pass over the position of these liberated particles. The potential well of CDM_1 will recapture gas particles expelled in the direction of its outbound path in a process similar to the capture of surrounding gas particles of the ICM in the later inbound motion of CDM_1 (see Fig. 19). This process will not take place at apocentre though, as the dark matter subclump CDM_1 reaches its extremal x and y-position and does not later affect gas particles ejected at this point.

The simulation shows that the restoring gravitational pull that one then expects from the dark matter subclump CDM_1 is not sufficient to recollect the gas particles which have been pushed away at apocentre. This is because gas particles can be expelled far enough from the local potential well in comparison to its depth (there is more than 0.5 Mpc between the bottom of the local gravitational potential in the right panel of Fig. 19). In addition, there is no time for a restoring pressure force to develop, as tracing the high pressure particles selected at $z = 0.12$ (the black set of points in both panels of Figure 19) shows that a fraction of the surrounding gas particles of CDM_1 , which are not part of CG_1 , rapidly fall back into the local potential well of CDM_1 . This happens as CDM_1 moves back towards the cluster centre and pressure equilibrium is again achieved for the gas trapped in the local potential well of CG_1 . The particles of CG_1 which have been left over in an environment of weaker gravitational potential will quickly expand adiabatically to equilibrate with the surrounding pressure of the ICM which is much less dense. In this rapid process ($z = 0.16 \rightarrow 0.12$), they cool down from the already low temperature they have as former sub-clump core, and appear as cold fronts in the above temperature maps. However, the majority of CG_1 particles are not expelled from the local potential of CDM_1 : as these particles reach the cluster centre in the second core passage they produce the secondary compression/bow shocks.

We have neglected pressure gradients in this discussion. Pressure gradients will add to the inertial effects which we have focused on and will obviously amplify the phenomenon. Also, ram pressure stripping will contribute to unbinding some of the gas of CG_1 when its velocity is large in the surrounding ICM and may also introduce internal motions in the dense regions of the gas which can result in patterns observationally very similar to cold fronts (Heinz et al. 2003). Because our cold fronts do not develop when the clump velocity is maximal, and because we do not have sufficient resolution to resolve internal motions in the very core of CG_1 , it seems unlikely that ram pressure effects play a major role are responsible in the formation of the cold fronts in our simulations.

A more detailed, quantitative approach and a precise assessment of the relative importance of pressure gradients and ram pressure stripping compared to the the ‘‘inertial’’ pressure effect we discussed will be addressed in future work.

6.3 Comparison to other work

In this paragraph, we briefly put this mechanism in the perspective of similar work addressing the formation of cold

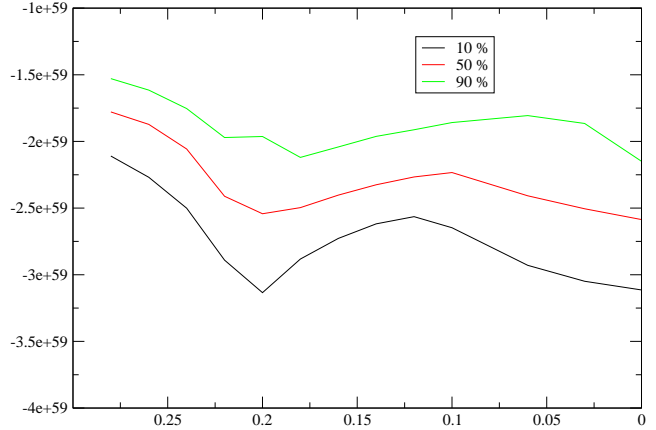


Figure 17. Total energy T of the CG_1 particles as a function of redshift, from $z = 0.28$. The black, red and green curves respectively give the 10, 50 and 90% quartiles of the distribution. The abscissa is the y-axis in the simulation and the ordinate is the energy (in erg).

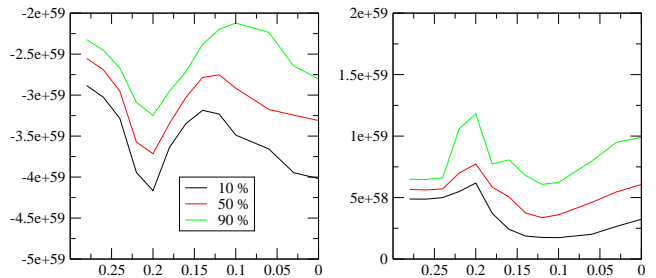


Figure 18. Same as Fig. 17 but for the potential W and internal energy U (left and right panels) of the CG_1 particles as a function of redshift. The black, red and green curves respectively give the 10, 50 and 90% quartiles of the distribution.

fronts using hydrodynamical simulations that has been carried out by Bialek et al. (2002); Nagai & Kravtsov (2003); Heinz et al. (2003).

Bialek et al. (2002) have reached conclusions similar to ours as they considered the development of a cold front in a major cluster merger, arguing that adiabatic expansion of the subcluster gas core as it is freed from its local

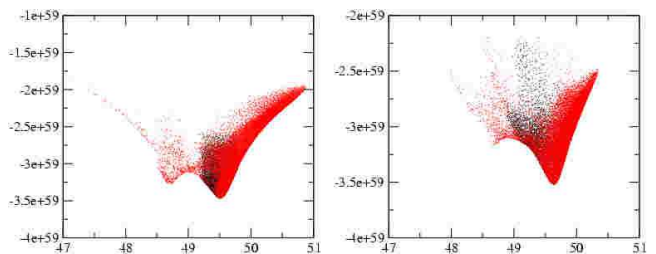


Figure 19. Y positions (in Mpc) of the CG_1 particles (in red) in the gravitational potential W created by the DM of the whole cluster. The black points give the positions of the pressure-selected particles (by their Compton y parameter at $z = 0.1$, see 5.2). The right and left panels correspond to $z = 0.16$ and $z = 0.12$ respectively. A better, high resolution version of this figure is available at: <http://www-astro.physics.ox.ac.uk/~hxm/ColdFronts/>.

gravitational potential could lead to a cold front. We have performed a detailed check of their statement that this expansion is coupled with compression and heating of the less dense cluster gas in forward of the ablated core. Upstream compression and heating are the result of the bow shock induced by the motion of the core. Expansion and further cooling of part of the dense cold subcluster core gas at the apocentre of its orbit lead to the cold front.

Nagai & Kravtsov (2003) have shown using temperature and pressure cuts through the ICM that the motion of the subcluster core gas in the ambient cluster gas drives a shock in front of their simulated cold front during a major merger. Confirming that this shock enhances the density and temperature gradients between the surrounding ICM and the cold gas of the subcluster core, they viewed their cold front as that part of this gas which is “sloshed out” of its local dark matter gravitational potential well. We have clarified this part of the picture by tracing back the gas particles of one of our simulated cold fronts. According to Nagai & Kravtsov (2003), rapid motion of the cold gas inside the freshly shocked gas could result in the sharp boundary. Our simulations rather show that the role of sloshing in the formation of the cold fronts is significantly amplified at the apocentres of the orbits of each of the subcluster cores, where our cold fronts develop. We have also noted that the velocity of the gas flow over the boundaries of our cold front is smooth, confirming the claim of Nagai & Kravtsov (2003) that the gas of the front appears to be moving together with its surrounding hot gas. This is different from the contact discontinuity model discussed by Vikhlinin & Markevitch (2002) and suggests either that there is not enough resolution in the simulations or that the Vikhlinin & Markevitch (2002) picture of cold gas surrounded by a uniform wind of hot gas is not fully appropriate.

Heinz et al. (2003) have employed 2D eulerian simulations to study the evolution of a cold gas core as it experiences ram pressure stripping when immersed in a background uniform flow of hot gas (the flow is switched on at the beginning of the simulations). Their cold gas core is assumed in hydrostatic equilibrium in a local, fixed, gravitational potential. Heinz et al. (2003) pointed out that gas motions inside the cold core are mainly induced by two processes: (1) developing Kelvin-Helmoltz instabilities, as part of the external regions of the cold gas core is driven downstream, away from the core as well as (2) the displacement of the bulk of the gas core downstream from the centre of the local gravitational potential because of ram pressure. Both processes result in a vortex forming inside the gas core. This vortex brings low entropy material from the densest parts of the gas core to its upstream boundary, where it can adiabatically expand and cool, leading to the formation of the cold front. Heinz et al. (2003) intentionally employed a uniform background flow, a fixed local gravitational potential, and no global gravitational potential to simplify the picture and focus on the hydrodynamics. In fact, ram pressure stripping will also play a role in the development of the cold fronts in our simulations. However, we have presented evidence that the interplay between the dynamics of the subcluster dark matter and gas cores (as embedded in the global potential well of the newly formed cluster) might be the essential ingredient to the formation of cold fronts in massive cluster mergers.

7 CONCLUSION

Recent high-resolution X-ray observations by *Chandra* have shown that cold fronts are a very common feature of the ICM of bright clusters. Cold fronts have been mainly interpreted as a by-product of mergers, yet without any clear-cut description of their physical origin.

We have simulated a late-forming massive merger resulting in a $1.4 \times 10^{15} M_{\odot}$ cluster in a concordance cosmological background using a hydrodynamical description that is only adiabatic, but which is suitable to bring out the Lagrangian origin of the bulk of the cold fronts. This sheds light on the details of the formation process of the cold fronts.

We have first shown that high-resolution SPH simulations can provide temperature maps of an accuracy comparable to that achieved with state-of-the-art Eulerian codes, and can be used to study the formation and evolution of the ICM during a massive merger. In particular, we have singled out the initial compression of the gas intervening between the cores of the merging sub-clumps as they move towards their first encounter, the generation of two centrally symmetric bow shocks as these cores have moved beyond their first passage, the outwards propagation of the shock together with the simultaneous formation of cold fronts, and the secondary compression of intervening gas before the final merging of the cores. Some of the X-ray temperature maps of the post-merger ICM are strikingly similar to those presented in, e.g. Markevitch et al. (2002b).

We have then focused on the bow shocks sweeping through the ICM, noting that they may have interfered with previous shocks developing in the central region of the cluster before first core passage. We have found that in a 500 kpc thick slice roughly containing the plane of merging of the two cores, they affect most of the ICM and keep on extending from their central generation at $z = 0.22$ down to $z = 0$, first as shocks, later on as pressure waves. Eventually they reach beyond the 3.4 Mpc virial radius of the cluster. Even if they weaken from $z = 0.12$ on, these features can affect the external underdense IGM or the filaments and interfere with accretion shocks. They may significantly contribute to gas stripping late-type galaxies populating the ICM, and can lead a fraction of the ICM to escape the global gravitational potential as a result of the pressure wave dissipating energy in the outskirts of the cluster.

Finally, we have considered in detail the formation of one of the two symmetric cold fronts. The front develops in the wake of the merger/bow shock as some of the cold gas associated with one of the dense cores of the sub-clumps which has been heated at core passage is freed from its local gravitational potential well. This occurs as the sub-clump core reaches the apocentre of its eccentric orbit and starts to move back towards second passage.

At this point, ram pressure stripping is minimal, but the accelerated motion transforms global pressure into an effective force pointing outwards, acting on the gas component of the clump in opposite directions to the gravitational pull from the clump of dark matter and from the whole cluster. As a result, some of this gas is liberated from the local gravitational well, decouples from the dark matter, and quickly cools as it expands adiabatically to achieve pressure equilibrium with its surrounding.

This process has to be compared to, for instance, the

pure ram-pressure stripping effect advocated by Heinz et al. (2003) for the formation of some of the cold fronts. Even if ram pressure stripping seems marginal to the formation of our two simulated cold fronts, we would like to precisely assess the relative importance of the two processes for cold front formation as a function of the mass ratio between the merging subclusters in simulations including gas and dark matter in future work.

Confirming Nagai & Kravtsov (2003), we find that the velocity field is continuous all over the cold front up to the preceding shock, down to the resolution where we have sampled the velocity field (~ 80 kpc). Higher resolution than we have used is needed to address the question of persistence of the cold front interface against fluid instabilities. While the bow shock/pressure wave keeps on extending, it begins to dissolve at $z = 0.12$, however our cold fronts remain stable over a longer period, down to $z = 0.03$ when they start to mix with the hotter ICM. We find that they are little affected by the secondary shocks generated at core passage and final inspiralling.

Finally, SZ polarisation of the CMB combined with the kinetic SZ effect has been brought in as a promising tool to constrain the projected velocity of the ICM. We have checked in mock SZ polarisation maps that our cold fronts developing on a plane orthogonal to the line of sight do not contribute any significant signal, a consequence of their low bulk velocity with respect to the surrounding ICM compared to that of subcluster cores.

All figures are available at high resolution at the URL : <http://www-astro.physics.ox.ac.uk/~hxm/ColdFronts/>

ACKNOWLEDGEMENTS

We thank Greg Bryan for useful comments. JMD is supported by a Marie Curie Fellowship of the European Community programme *Improving the Human Research Potential and Socio-Economic knowledge* under contract number HPMF-CT-2000-00967. HM acknowledges financial support from PPARC.

REFERENCES

- Bialek J. J., Evrard A. E., Mohr J. J., 2002, ApJL, 578, 9
 Fujita Y., Sarazin C. L., Nagashima M., Yano T., 2002, ApJ, 577, 11
 Heinz S., Churazov E., Forman W., Jones C., Briel U. G., 2003, preprint, astro-ph/0308131
 Keshet U., Waxman E., Loeb A., Springel V., Hernquist L., 2003, ApJ, 585, 128
 Markevitch M., Gonzalez A. H., David L., et al., 2002a, ApJL, 567, 27
 Markevitch M., Ponman T. J., Nulsen P. E. J., Bautz M. W., Burke D. J., David L. P., 2000, ApJ, 541, 542
 Markevitch M., Vikhlinin A., 2001, ApJ, 563, 95
 Markevitch M., Vikhlinin A., Forman W. R., 2002b, in *Matter and energy in clusters of galaxies*, edited by S. Bowyer, C.-Y. Hwang, vol. X of ASP conference series
 Mazzotta P., Markevitch M., Vikhlinin A., Forman W. R., David L. P., VanSpeybroeck L., 2001, ApJ, 555, 205
 Nagai D., Kravtsov A. V., 2003, ApJ, 587, 514
 Ricker P. M., Sarazin C. L., 2001, ApJ, 561, 621
 Roettiger K., Loken C., Burns J. O., 1997, ApJS, 109, 307
 Springel V., Hernquist L., 2002, MNRAS, 333, 649
 Springel V., Yoshida N., White S. D. M., 2001, New Astronomy, 6, 79
 Sun M., Murray S. S., Markevitch M., Vikhlinin A., 2002, ApJ, 565, 867
 van de Weygaert R., Bertschinger E., 1996, MNRAS, 281, 84
 Vikhlinin A., Markevitch M., Murray S. S., 2001, ApJ, 551, 160
 Vikhlinin A. A., Markevitch M. L., 2002, AstL, 28, 495
 Voit G. M., Balogh M. L., Bower R. G., Lacey C. G., Bryan G. L., 2003, preprint, astro-ph/0304447

This paper has been produced using the Royal Astronomical Society/Blackwell Science L^AT_EX style file.